J. Fluid Mech. (2010), *vol.* 660, *pp.* 197–220.
doi:10.1017/S002211201000265X

Aeromechanics of passive rotation in flapping flight

J. P. WHITNEY† AND R. J. WOOD

School of Engineering and Applied Sciences, Harvard University, Cambridge, MA 02138, USA

(Received 5 June 2009; revised 7 January 2010; accepted 4 May 2010;
first published online 27 July 2010)

Flying insects and robots that mimic them flap and rotate (or 'pitch') their wings with large angular amplitudes. The reciprocating nature of flapping requires rotation of the wing at the end of each stroke. Insects or flapping-wing robots could achieve this by directly exerting moments about the axis of rotation using auxiliary muscles or actuators. However, completely passive rotational dynamics might be preferred for efficiency purposes, or, in the case of a robot, decreased mechanical complexity and reduced system mass. Herein, the detailed equations of motion are derived for wing rotational dynamics, and a blade-element model is used to supply aerodynamic force and moment estimates. Passive-rotation flapping experiments with insect-scale mechanically driven artificial wings are conducted to simultaneously measure aerodynamic forces and three-degree-of-freedom kinematics (flapping, rotation and out-of-plane deviation), allowing a detailed evaluation of the blade-element model and the derived equations of motion. Variations in flapping kinematics, wing-beat frequency, stroke amplitude and torsional compliance are made to test the generality of the model. All experiments showed strong agreement with predicted forces and kinematics, without variation or fitting of model parameters.

Key words: dynamic stall, flow–structure interactions, swimming/flying

1. Introduction

There has been substantial interest in flapping-wing propulsion over the past few decades due to potential energetic and agility benefits over fixed-wing flight. This interest is also motivated by the numerous open research questions related to unsteady flow and the aeroelastic response of flapping wings. This is particularly true of insect flight, for which there is evidence of significant aeroelastic effects in both the local deformations of the airfoils (Daniel & Combes 2002) and the gross rotation ('pitching') of wings about the torsional axis (Ennos 1988*a*; Bergou, Xu & Wang 2007). This paper exclusively focuses on the latter case, with wings modelled as thin rigid bodies. This assumption is appropriate for many, but certainly not all, insect and robotic wings.

It is almost certain that insects directly exert rotational moments to actively control wing rotation, as they possess musculature so able (Dudley 2000). However, it is an open question whether or not these muscles provide a significant amount of the power required to flip the wing during 'nominal' flapping, or whether they are used only to apply small corrections to the wing's trajectory for control purposes.

† Email address for correspondence: jwhitney@fas.harvard.edu

For some insects, there is direct evidence of passive rotation from observations of torsional waves that begin at the tip rather than the base of a wing (Ennos 1988*b*). In addition, aerodynamic estimates have shown that it is possible to achieve rotation purely by passive means for some insects (Bergou *et al.* 2007), but there is insufficient evidence to make this claim for all insects. For a mechanical device, relying on passive rotation is not an inevitability, but a design choice.

While it is not possible to claim, in general, that passive rotation is the most efficient flapping configuration, its observation in nature, reduced complexity and success in robotic insects (Wood 2008) strongly warrants further study. This paper develops the passive-rotation equations of motion and models aerodynamic forces and moments using a blade-element approach. However, the simplifications of the blade-element method present many uncertainties, and experiments are needed to validate its applicability. These experiments must measure and correlate wing forces and kinematics for passively rotating wings.

Experiments in the literature reporting measurements of wing forces and kinematics are numerous. Dickinson, Lehmann & Sane (1999) used a Reynolds-number-matched fruit-fly (*Drosophila melanogaster*) wing model to measure time-varying aerodynamic forces and correlate them to three-degree-of-freedom flapping kinematics. Fry, Sayaman & Dickinson (2003) and Ristroph *et al.* (2009) used hull-reconstruction techniques to measure the three-dimensional wing trajectories, and body trajectories, of free-flying *Drosophila*. Walker, Thomas & Taylor (2009) used photogrammetric reconstruction to measure complete wing trajectories, including higher order deformations, of locusts (*Schistocerca gregaria*) and hoverflies (*Eristalis tenax*) in a wind tunnel. Graetzel *et al.* (2008), in experiments with *Drosophila*, used a single high-speed video camera to extract the projected flapping angle, while simultaneously measuring vertical forces using a silicon micromachined capacitive force sensor.

The experiments reported here use high-speed video stereophotogrammetry to measure three-degree-of-freedom kinematics (flapping, rotation and out-of-plane motion). Forces are measured, in real time, using a capacitive-based force sensor. Artificial wings, with varying torsional compliance, are flapped at different frequencies and amplitudes and allowed to rotate passively. The measured forces and kinematics provide a direct assessment of the blade-element assumptions, and evaluation of the derived equations of motion for several test cases. The quantitative agreement is very good, validating both the wing dynamics model and the continued and expanded use of the experimental set-up for studying at-scale flapping-wing aerodynamics.

2. Aeromechanics

2.1. *Wing morphology*

Passive-rotation characteristics have a strong dependence on the detailed shape and mass distribution of a wing. Natural and artificial wings display great variation in size, planform, material composition and vein structure (Daniel & Combes 2002). Development of a concise wing parametrization is required. The commonly used definitions by Ellington (1984) provide a starting point in the formulation of a complete parametrization.

Figure 1 illustrates a generic wing planform. The x-axis is aligned with the wing's axis of rotation (torsional axis), where r is the radial distance along it. The intersection of the x-axis and y-axis (O') shall be called the shoulder. Typically, the wing root – defined as the most proximal point on the leading edge – is not coincident with the

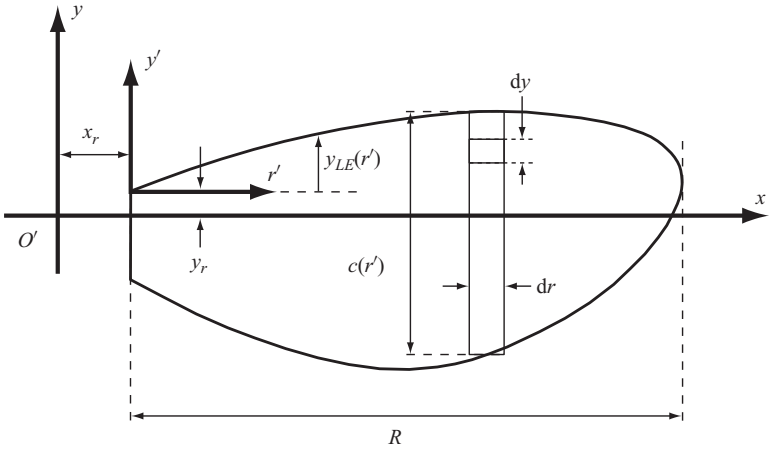

FIGURE 1. Coordinates and dimensions for a generic insect wing planform. Differential elements for radial and chordwise integration are shown.

shoulder. The radial distance from the wing root, along the r'-axis, is r'. The wing-root offsets x_r and y_r are labelled in figure 1.

The wing length, R, is defined here as projected distance along the r'-axis from the wing root to the most distal point on the wing. The mean chord, $\bar{c}$, is defined as the area of one wing divided by the wing length, A_w/R. Radial coordinates may be made non-dimensional by R and chordwise coordinates by $\bar{c}$ (Ellington 1984). Resulting values are radial distance (relative to root) $\hat{r} \equiv r'/R$, chord profile $\hat{c} \equiv c/\bar{c}$, leading-edge profile $\hat{y}_{LE} \equiv y_{LE}/\bar{c}$, x-root offset $\hat{x}_r \equiv x_r/R$ and y-root offset $\hat{y}_r \equiv y_r/\bar{c}$. Passive-rotation dynamics depend critically on the shape of the leading edge, as this alters the chordwise location of the centre of lift. It is customary to define the wing's aspect ratio as $\mathcal{AR} \equiv R/\bar{c}$. A wing's shape can be fully specified by R, $\mathcal{AR}$, $\hat{c}(\hat{r})$ and $\hat{y}_{LE}(\hat{r})$. The choice of R as the sole dimensional parameter was arbitrary – $\bar{c}$ or A_w could serve equally. In addition, the offset parameters $\hat{x}_r$ and $\hat{y}_r$ define the hinge location. Frequently, it is convenient to define $\hat{x}_r = 0$ and fold any radial offset into $\hat{c}(\hat{r})$.

While the wing shape has been fully specified and non-dimensionalized, it still contains two arbitrary shape functions, $\hat{c}(\hat{r})$ and $\hat{y}_{LE}(\hat{r})$. This is not a drawback when analysing one specific wing, but it is highly desirable to reduce these functions to a small number of constant parameters, which capture only the essential nature of the wing's shape. This can be accomplished in part by defining radius moments (see Ellington 1984) of the form

$$\hat{r}_k^k \equiv \int_0^1 \hat{c}\,(\hat{r})\,\hat{r}^k\,\mathrm{d}\hat{r}, \tag{2.1}$$

where the subscript is the moment index and the superscript is an exponent. These parameters can be dimensionalized by multiplying by the wing length. The first-order radius moment, $r_1 = R\hat{r}_1$, is the wing's centre of area. Higher order moments describe the area distribution of the wing. For insect wings, there is a strong correlation between $\hat{r}_1$ and $\hat{r}_2$. The analytical relationship

$$\hat{r}_2 = 0.929\,(\hat{r}_1)^{0.732} \tag{2.2}$$

was found to closely fit experimental measurements from insect wings of all shapes and sizes (Ellington 1984). A beta distribution can be used to reconstruct the non-dimensional wing shape:

$$\hat{c} = \hat{r}^{p-1}(1-\hat{r})^{q-1}/B(p,q), \tag{2.3}$$

where $B(p,q)$ is the beta function, which is given by

$$B(p,q) = \int_0^1 \hat{r}^{p-1}(1-\hat{r})^{q-1}\,\mathrm{d}\hat{r}. \tag{2.4}$$

If the beta-function parameters are chosen as

$$p = \hat{r}_1\left(\frac{\hat{r}_1(1-\hat{r}_1)}{\hat{r}_2^2-\hat{r}_1^2}-1\right), \tag{2.5}$$

$$q = (1-\hat{r}_1)\left(\frac{\hat{r}_1(1-\hat{r}_1)}{\hat{r}_2^2-\hat{r}_1^2}-1\right), \tag{2.6}$$

then the first and second radial moments of (2.3) will be $\hat{r}_1$ and $\hat{r}_2$. Measurements from a wide range of insects, in both species and scale, were made and have been shown to match this distribution to within 5 % (Ellington 1984). Combined with the relationship given in (2.2), the non-dimensional radial-area distribution of many insect wings, $\hat{c}(\hat{r})$, can be completely determined from a single constant parameter, the non-dimensional radial location of the wing's centre of area, $\hat{r}_1$.

The variety in insect wing shapes is not only due to variations in $\hat{r}_1$ (which ranges from 0.4 to 0.6), but also due to their many different leading-edge profiles. An attempt at parametrizing $\hat{y}_{LE}$ is not known at this time, but would be helpful in analysing the importance of leading-edge shape in passive-rotation dynamics as well as aerodynamic efficiency in general.

2.2. *Flapping kinematics*

Figure 2 shows coordinate systems and angles necessary for a basic description of the rigid-wing flapping kinematics of most insects. A left wing is shown close to the end of its downstroke. The $X'Y'Z'$-coordinate frame has its origin O' at the shoulder of the left wing. The X'-axis is normal to the mean stroke plane, with the Y'-axis pointing in the right lateral direction. The Z'-axis points in the ventral direction. The xyz-axes are wing-fixed. These are the same axes as shown in figure 1, though here they are shown offset, next to the wing hinge, for clarity. It is important to place the xyz-frame at O' when calculating moments of inertia.

The $x''y''z''$-axes rotate with the flapping angle ϕ, defined as the angle between the negative Y'-axis and the x''-axis, where the axis of rotation is the negative X'-axis. The $x'y'z'$-axes (not to be confused with the $r'y'$-axes in figure 1) rotate with the flapping angle and with the stroke-plane-deviation angle, θ, defined as the angle between the x''-axis and the x-axis, where the axis of rotation is the z''-axis. The rotation angle, ψ, is defined as the angle between the y'-axis and the y-axis, rotating about the x-axis. The total angular velocity of the wing is the sum of flapping, deviation and rotation:

$$\boldsymbol{\omega} = -\dot{\phi}\boldsymbol{e}_{X'} + \dot{\theta}\boldsymbol{e}_{z''} + \dot{\psi}\boldsymbol{e}_x. \tag{2.7}$$

In the wing-bound frame, this becomes

$$\boldsymbol{\omega} = (\dot{\psi} - \dot{\phi}\sin\theta)\boldsymbol{e}_x + (-\dot{\phi}\cos\theta\cos\psi + \dot{\theta}\sin\psi)\boldsymbol{e}_y + (\dot{\phi}\cos\theta\sin\psi + \dot{\theta}\cos\psi)\boldsymbol{e}_z. \tag{2.8}$$

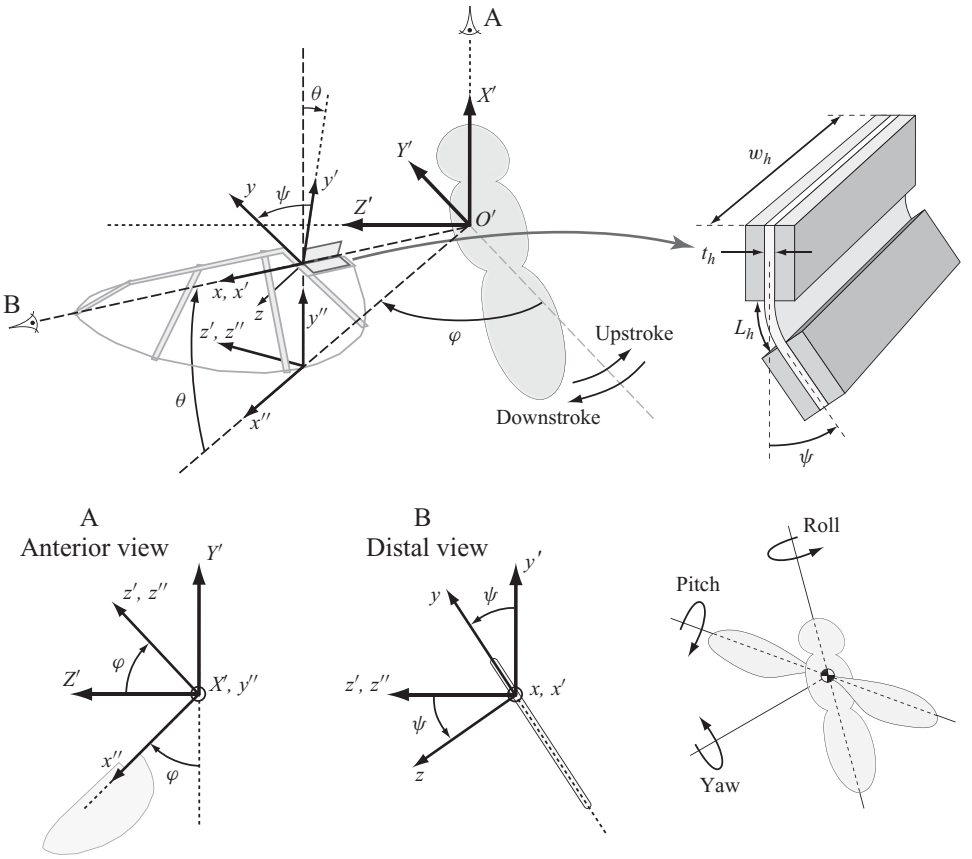

FIGURE 2. Coordinate systems and angles used to specify wing kinematics, shown for a left wing and vertical-body orientation. All coordinate frames share the same origin, O' – they are shown offset here only for clarity. A robotic insect using passive rotation may have a wing flexure hinge of the type shown. The driving spar (flapping input) mounts to the top link of the hinge, the wing to the bottom.

It is useful to define the velocity of the hinge line, $\boldsymbol{v}_h$. The hinge has no radial velocity component

$$\boldsymbol{v}_h = V_0 \boldsymbol{e}_y + W_0 \boldsymbol{e}_z, \tag{2.9}$$

and is defined by $\boldsymbol{\omega}_h \times r\boldsymbol{e}_x$, where $\boldsymbol{\omega}_h$ is given by $\boldsymbol{\omega} - \omega_x \boldsymbol{e}_x$. The inertial and virtual mass moments depend (see below) on the acceleration of the wing at the hinge, which is given by

$$\begin{aligned} \dot{\boldsymbol{v}}_h &= \dot{V}_0 \boldsymbol{e}_y + \dot{W}_0 \boldsymbol{e}_z \\ &= \dot{\boldsymbol{\omega}}_h \times r\boldsymbol{e}_x + \boldsymbol{\omega}_h \times \boldsymbol{v}_h \\ &= r(\dot{\omega}_z + \omega_x \omega_y)\boldsymbol{e}_y + r(-\dot{\omega}_y + \omega_x \omega_z)\boldsymbol{e}_z. \end{aligned} \tag{2.10}$$

Aerodynamic forces and moments are not directly related to the angle of rotation ψ, but rather to the angle of attack, α, which is defined as the angle between the wing chord and the instantaneous local velocity:

$$\alpha = \text{atan2}(-\omega_y, \omega_z). \tag{2.11}$$

This definition gives α a right-hand-rule sign convention relative to the x-axis.

2.3. *Wing hinge*

For insect-scale flapping-wing robots, passive rotation can be achieved by attaching the wing to the driving spar with an elastic hinge (Wood 2007). Figure 2 shows a hinge near the base of the wing. The hinge stiffness is controlled by adjusting the geometry and material of a flexible polymer layer sandwiched between rigid structural layers. The rotational stiffness is approximated by that of a linear elastic beam deforming under an external moment:

$$\kappa_h = \frac{E_h t_h^3 w_h}{12 L_h}, \tag{2.12}$$

where t_h, w_h and L_h are the thickness, width and length of the central layer, and E_h is the modulus. For all experiments presented here, L_h has sufficient length to prevent the top and bottom structural portions of the hinge from colliding when the wing is rotated maximally.

2.4. *Passive-rotation equations of motion*

Insect wings flex and deform when flapped, as a result of their distributed radial and chordwise compliance (cf. Daniel & Combes 2002). However, if these deflections are small, assuming rigid-body motion of the entire wing is greatly simplifying. With the wing shoulder as an origin, the motion of the wing is entirely rotational. Under these assumptions, the Euler equations are the governing equations of motion. The inertia tensor is defined here as

$$I_{jk} = \int_V \rho_w(\boldsymbol{r})\,(r^2\delta_{jk} - x_j x_k)\,\mathrm{d}V, \tag{2.13}$$

where $\rho_w(\boldsymbol{r})$ is the wing density and $\boldsymbol{r}$ is the displacement vector for the xyz-axes. The Euler equation describing rotation about the x-axis is

$$M_x = I_{xx}\dot{\omega}_x - (I_{yy} - I_{zz})\omega_y\omega_z + I_{xy}(\dot{\omega}_y - \omega_x\omega_z) + I_{yz}\left(\omega_y^2 - \omega_z^2\right) + I_{xz}(\dot{\omega}_z + \omega_x\omega_y), \tag{2.14}$$

where M_x is the sum of all external moments about the x-axis. For a wing of characteristic thickness t_w, assuming a thin wing ($t_w \ll \bar{c}$, R) allows the simplification $I_{xz} = I_{yz} = 0$, and, by the perpendicular-axis theorem, $I_{xx} + I_{yy} = I_{zz}$, resulting in the simplified rotational equation of motion

$$M_x = I_{xx}(\dot{\omega}_x + \omega_y\omega_z) + I_{xy}(\dot{\omega}_y - \omega_x\omega_z). \tag{2.15}$$

In the absence of out-of-plane motion ($\theta = \dot{\theta} = 0$), this simplifies to

$$I_{xx}\ddot{\psi} = M_x + I_{xy}\ddot{\phi}\cos\psi + \tfrac{1}{2}I_{xx}\dot{\phi}^2\sin 2\psi, \tag{2.16}$$

where the kinematic variables have been substituted using (2.8). The net externally applied moment about the x-axis, M_x, includes aerodynamic moments and the elastic restoring moment from the wing hinge. It would also include direct rotational input torques by the insect or robot.

The second terms on the right-hand sides of (2.16) and (2.15) are the 'inertial' moment that results when the wing hinge line does not pass through the centre of mass of the wing, helping to 'flip' the wing when it is accelerated. With the hinge acceleration given by (2.10), note in (2.15) that $\dot{\omega}_y - \omega_x\omega_z = -\dot{W}_0/r$. This 'inertial flip' term is proportional to the angular acceleration normal to the instantaneous stroke plane.

Given $\phi(t)$, $\theta(t)$, a model for the aerodynamic torque, a model for the elastic wing hinge and the inertia components I_{xx} and I_{xy}, (2.15) is simply integrated in time to determine the passive-rotation response, $\psi(t)$.

2.5. *Aerodynamics*

A passive-rotation simulation requires a model of the aerodynamic forces and moments exerted on the wing. The Reynolds number for flapping flight may be defined as

$$Re \equiv \frac{\bar{u}\bar{c}}{\nu}, \tag{2.17}$$

where $\bar{u}$ is the mean translational velocity of the wing tip and ν is the kinematic viscosity of air. The mean translational velocity is given by $2\Phi f R$, where Φ is the total flapping angular amplitude (peak-to-peak) and f is the flapping frequency. Most insects have a Reynolds number in the range 100–1000, though some are as low as 10 or as high as 10 000 (Ellington 1984).

Flapping kinematics are characterized by large angles of attack and high rates of rotation. Massive separation of boundary layers, possible reattachment and strong vortex shedding at both the leading and trailing edges are possible features of this type of flow. The wing also interacts with its own wake, especially in hover, potentially leading to significant time-dependent aerodynamic forces. Many different aerodynamic effects have been identified, and are reviewed by Sane (2003). Often, experiments attempt to explain the aerodynamics for a single wing at a single operating point, usually with the aim of identifying the important aerodynamic mechanisms for a particular insect species. Recent work by Lentink & Dickinson (2009) reverses this trend; they investigate aerodynamic performance under the systematic variation of (effectively) wing aspect ratio, *Re* and flapping amplitude.

Two- and three-dimensional computational fluid dynamics (CFD) calculations are an alternative to flapping experiments (Wang 2000; Wu & Sun 2004; Young *et al.* 2009). They provide detailed information not only on the forces and moments, but also on the structure of the wake and surrounding fluid. Published calculations show good general agreement with experiments. Two-dimensional CFD calculations can now be run fast enough, on supercomputers, to perform design and optimization studies (Pesavento & Wang 2009). Two-dimensional CFD-based passive-rotation optimization studies are probably feasible.

Whether aerodynamic force and moment data come from computation or experiment, a reduction to non-dimensional form is highly desirable. A proper reduction will allow the data to be applied as broadly as possible. The blade-element method is a quasi-static technique for applying non-dimensional experimental and computational results to similar operating conditions. The success of this method is critically limited by the quality of the force and moment coefficients and its quasi-static assumptions.

2.6. *Blade-element method*

Lift and drag coefficients provide a convenient way to apply computational or experimental results to different operating conditions or configurations. The general form of an aerodynamic force coefficient is

$$C_F = \frac{F}{qS}, \tag{2.18}$$

where F is the force in question, q is the dynamic pressure and S is a reference area. The dynamic pressure is defined as $(1/2)\rho V^2$, where ρ and V are the reference

air density and velocity, usually the free-stream values. The reference area is usually the area over which the force acts or an area characteristic to the body. A constant force coefficient is not sufficient to predict forces for all flow conditions. For example, aerodynamic force coefficients may be a function of the Mach number and the Reynolds number (Re). If the relevant forces are a weak function of these parameters, using an off-condition coefficient (slightly different geometry, different size, etc.) can still give a reasonable prediction of force magnitudes.

The blade-element method is simply the application of (2.18) to chordwise strips along a flapping wing. Figure 1 shows a sample wing strip. The wing must be divided into strips because the local velocity varies along the wing. For the decidedly subsonic insect flapping regime, force coefficients should vary with α, Re and wing shape. Ideally, these variations will be clear trends that experiments can identify. If force (or moment) coefficients begin to vary with the details of the flapping kinematics, or if they depend on products of these changes, the usefulness of the blade-element method is reduced severely.

The blade-element method estimates forces based only on instantaneous flow conditions, making the method quasi-static. Unsteady flow features, such as wake capture, cannot be modelled directly. They may enter indirectly, for example, if the force coefficient is a function of α, and the time-dependent force appears periodically, with the time of occurrence corresponding to a particular α. However, if the flapping motion becomes aperiodic, such as during a manoeuvre, or if the periodic flapping kinematics are changed significantly, then the previously tailored α-dependence will produce erroneous results.

2.6.1. *Aerodynamic forces*

In hover, the ambient air velocity is negligible; so the dynamic pressure on the wing develops only through its relative motion. Thus, the aerodynamic force components on each chordwise strip can be expressed as

$$\mathrm{d}F_{aero} = \underbrace{\tfrac{1}{2}\rho\omega_h^2(r' + x_r)^2}_{q}\,\underbrace{C_F(\alpha)}_{C_F}\,\underbrace{c(r')\,\mathrm{d}r'}_{\mathrm{d}S}, \tag{2.19}$$

which is simply a rearranged form of (2.18). When there is no stroke-plane deviation, $\omega_h = -\dot{\phi}$.

The total aerodynamic force is commonly decomposed into lift and drag components, F_L and F_D. Drag is directed in opposition to the relative ambient velocity, and lift orthogonal. Experiments and CFD calculations (Dickinson *et al.* 1999; Wang, Birch & Dickinson 2004) have shown consistent functional forms for the variation of lift and drag coefficients with α:

$$\left.\begin{aligned} C_L(\alpha) &= C_{L_{max}} \sin(2\alpha), \\ C_D(\alpha) &= \left(\frac{C_{D_{max}} + C_{D_0}}{2}\right) - \left(\frac{C_{D_{max}} - C_{D_0}}{2}\right)\cos(2\alpha). \end{aligned}\right\} \tag{2.20}$$

For the Reynolds number (≈100), geometry and flapping kinematics of a typical *Drosophila* wing, Dickinson *et al.* (1999) found by experiments that these coefficient

forms are best fit by

$$\left.\begin{aligned} C_{L_{max}} &= 1.8, \\ C_{D_0} &= 0.4, \\ C_{D_{max}} &= 3.4. \end{aligned}\right\} \tag{2.21}$$

These values are a common starting point for blade-element force estimates. Experiments or CFD simulations are used to refine them for specific wing shapes and Reynolds numbers.

Integrating (2.19) for the lift component leads to

$$F_L = \tfrac{1}{2}\rho\omega_h^2 C_L(\alpha)\bar{c}R^3 \underbrace{\int_0^1 (\hat{r}+\hat{x}_r)^2\,\hat{c}(\hat{r})\,\mathrm{d}\hat{r}}_{\equiv \hat{F}}, \tag{2.22}$$

where $\hat{F}$ is the non-dimensional aerodynamic force. The integral is easily performed to yield

$$\hat{F} = \hat{r}_2^2 + 2\hat{x}_r\hat{r}_1 + \hat{x}_r^2. \tag{2.23}$$

If $\hat{x}_r$ is zero (which can always be arranged), then the non-dimensional aerodynamic force is simply equal to $\hat{r}_2^2$. The drag force has an identical expression, the only difference being the coefficient. The unit vectors for lift, drag and the normal component of the aerodynamic force are defined as

$$\left.\begin{aligned} \boldsymbol{e}_L &= -\boldsymbol{e}_{\omega_h}, \\ \boldsymbol{e}_D &= -\boldsymbol{e}_{v_h}, \\ \boldsymbol{e}_N &= -\operatorname{sgn}(\alpha)\,\boldsymbol{e}_z. \end{aligned}\right\} \tag{2.24}$$

These definitions take into account the chosen sign convention for α, and the sign conventions of C_L and C_D, as used in (2.20). The normal force coefficient is found by a simple rotation, $C_N = \cos(\alpha)C_L + \sin(\alpha)C_D$.

2.6.2. *Rotational-axis aerodynamic moment*

The aerodynamic moment about the axis of rotation (x-axis) is more complicated because the chordwise position of the centre of pressure depends on the instantaneous angle of attack and on the detailed shape of the leading edge. The required integral is

$$M_{x,aero} = \tfrac{1}{2}\rho\omega_h^2 C_N(\alpha)\int_0^R y_{cp}(r')(r'+x_r)^2 c(r')\,\mathrm{d}r', \tag{2.25}$$

where $y_{cp}(r')$ is the distance from the hinge line to the centre of pressure. Dickson *et al.* (2006) report experimental data on the location of the centre of pressure as a function of α, for *Drosophila*:

$$\hat{d}_{cp} = \frac{0.82}{\pi}|\alpha| + 0.05, \tag{2.26}$$

where α is in radians, and $\hat{d}_{cp}$ is the non-dimensional location of the centre of pressure, measured back from the leading edge (i.e. 0 for the leading edge and 1 for the trailing edge). In the xy-frame, the location of the centre of pressure for each strip is

$$y_{cp} = y_r + y_{LE}(r') - c(r')\hat{d}_{cp}. \tag{2.27}$$

Inserting into (2.25) yields

$$M_{x,aero} = \tfrac{1}{2}\rho\omega_h^2 C_N(\alpha)\bar{c}^2 R^3 \int_0^1 [\hat{y}_r + \hat{y}_{LE}(\hat{r}) - \hat{c}(\hat{r})\hat{d}_{cp}(\alpha)]\,(\hat{r} + \hat{x}_r)^2\,\hat{c}(\hat{r})\,\mathrm{d}\hat{r}. \tag{2.28}$$

Thus, the location of the net centre of pressure is

$$\hat{Y}_{cp} = \frac{\displaystyle\int_0^1 [\hat{y}_r + \hat{y}_{LE}(\hat{r}) - \hat{c}(\hat{r})\hat{d}_{cp}(\alpha)]\,(\hat{r} + \hat{x}_r)^2\,\hat{c}(\hat{r})\,\mathrm{d}\hat{r}}{\hat{F}}, \tag{2.29}$$

with the resulting rotational moment expression

$$\boldsymbol{M}_{x,aero} = -\,\mathrm{sgn}(\alpha)\tfrac{1}{2}\rho\omega_h^2 C_N(\alpha)\bar{c}^2 R^3 \hat{F}\hat{Y}_{cp}(\alpha)\boldsymbol{e}_x. \tag{2.30}$$

Calculating and measuring aerodynamic moments is notoriously more difficult than aerodynamic forces. The root of this problem is that moments are highly sensitive to changes in the location of the centre of pressure. For an insect wing, the distance between the torsional axis and the centre of pressure may only be 10 % of the mean chord; so even small changes in position have a large effect on the resulting moment.

2.6.3. *Rotational aerodynamic forces*

The aerodynamic force, described previously, sometimes called the 'translational' aerodynamic force, is not a function of the instantaneous rotation rate. The influence of rotation is felt only indirectly through the α-dependence of the force coefficients. There is evidence (Sane & Dickinson 2002) that independent 'rotational' forces exist, which are a function of the instantaneous rotation rate.

The original adopted model for these forces is that of a thin wing fluttering at low α, with the rotational forces arising from a coupling of translation and rotation. This force has the form

$$\mathrm{d}F_{rot} = \tfrac{1}{2}\rho\omega_x\omega_h c(r' + x_r)C_R(\alpha)c(r')\mathrm{d}r'. \tag{2.31}$$

Experiments (Sane & Dickinson 2002) have shown that C_R varies both with rotation rate (ω_x) and the location of the rotational axis ($\hat{y}_r$). This force is not included in any calculations presented here, primarily because improved predictions of lift force could not be realized, and contributions to rotational moment could not be measured. Future experimental investigations, should they investigate this force, especially for the purposes of passive rotation, must include direct measurements of rotational moments to calculate the centre of pressure of these rotational forces.

2.6.4. *Aerodynamic damping*

The aerodynamic forces and moments discussed so far provide limited rotational damping to the system. Passive-rotation experiments (§ 3.3) confirmed that without such a term, the predicted wing trajectories are severely under-damped. In addition, consider the pathological case of a wing rotating, but not flapping. Clearly, there will be aerodynamic moments exerted on the wing, though the translational and rotational aerodynamic force terms (see (2.22) and (2.31)) would predict none.

For this term, the relative velocity only due to rotation of the wing is considered. The relative air velocity is zero at the hinge axis and increases linearly away from it, as illustrated in figure 3. Using a dynamic pressure based on this velocity, it is straightforward to adapt (2.19) to form the rotational damping moment for a differential element as

$$\mathrm{d}(\delta M_{rd}) = -\tfrac{1}{2}\rho(\omega_x y)^2 C_{rd}|y|\mathrm{d}r'\mathrm{d}y, \tag{2.32}$$

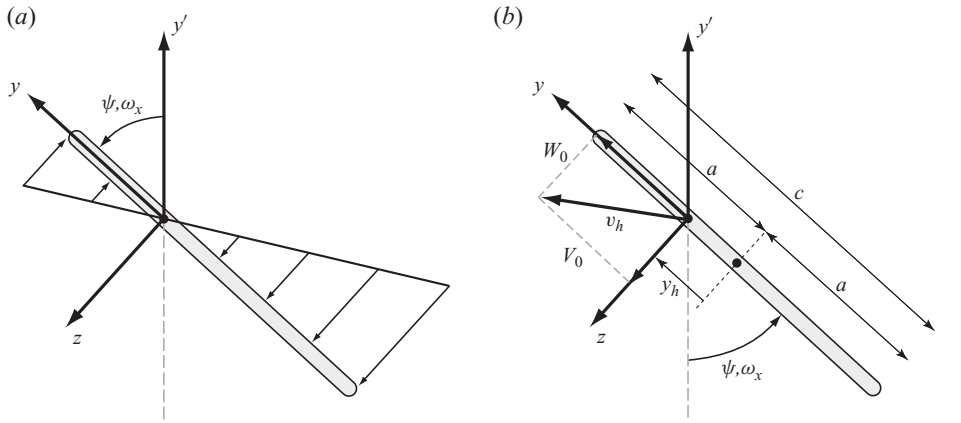

FIGURE 3. (*a*) A wing segment in pure rotation, and the resulting relative velocity profile seen by the wing. (*b*) The pertinent dimensions and variables for calculating the added-mass forces and moments.

where each chordwise strip is further divided (as in figure 1) into differential elements of height $\mathrm{d}y$, which are located at a distance y from the hinge axis. Integrating with respect to y yields δM_{rd}, the damping moment contribution from a single chordwise strip:

$$\delta M_{rd} = -\tfrac{1}{2}\rho\omega_x^2 C_{rd}\mathrm{d}r' \int_{y_0}^{y_1} |y| y^2 \,\mathrm{d}y, \tag{2.33}$$

$$= -\tfrac{1}{2}\rho\omega_x^2 C_{rd}\mathrm{d}r' \left(\tfrac{1}{4}|y_1|y_1^3 - \tfrac{1}{4}|y_0|y_0^3\right), \tag{2.34}$$

where

$$\left.\begin{aligned} y_0 &= y_r + y_{LE}(r) - c(r), \\ y_1 &= y_r + y_{LE}(r) \end{aligned}\right\} \tag{2.35}$$

are the coordinates of the trailing and leading edges of the wing. Switching to non-dimensional coordinates results in

$$\delta M_{rd} = -\tfrac{1}{2}\rho\omega_x^2 C_{rd}\bar{c}^4 R\hat{y}_{rd}(\hat{r})\,\mathrm{d}\hat{r}, \tag{2.36}$$

where

$$\hat{y}_{rd}(\hat{r}) = \tfrac{1}{4}[|\hat{y}_r + \hat{y}_{LE}|(\hat{y}_r + \hat{y}_{LE})^3 - |\hat{y}_r + \hat{y}_{LE} - \hat{c}|(\hat{y}_r + \hat{y}_{LE} - \hat{c})^3] \tag{2.37}$$

is the non-dimensional location of the effective moment arm of the rotational damping term for a single wing strip. Integrating these chordwise strips results in the total damping moment for the wing:

$$\boldsymbol{M}_{x,rd} = -\tfrac{1}{2}\rho\omega_x|\omega_x| C_{rd}\bar{c}^4 R\hat{Y}_{rd}\boldsymbol{e}_x, \tag{2.38}$$

where

$$\hat{Y}_{rd} = \int_0^1 \hat{y}_{rd}(\hat{r})\,\mathrm{d}\hat{r}. \tag{2.39}$$

This approach was also used by Andersen, Pesavento & Wang (2005) in experiments with tumbling cards. They used a rotational damping moment coefficient, C_{rd}, of 2.0, probably because this is the classical result for the two-dimensional drag coefficient

of a flat plate normal to a uniform flow. As the rotationally induced velocity is normal to the wing, it would be natural, in the present case, to use $C_{rd} = C_{D_{max}}$. For all calculations in this paper, a value of 5.0 was used. This value, in general, led to the best agreement between measured and predicted passive-rotation trajectories. However, the predictions were not highly sensitive to the exact value. All values of C_{rd} in the range 3–6 showed good agreement. The main challenge in determining it to higher precision is the difficulty in separating errors in the value of C_{rd} from errors in the location of the centre of pressure. Experiments that explicitly measure the moment about the rotational axis are likely to be required to better clarify the magnitude and variation of this parameter.

If the rotational axis does not pass through the chord centre, a net force will also result. For all calculations in this paper, these forces were neglected. The main reason is one of complexity. It is easy to quickly amass several coefficients which may be 'tuned' for a specific experimental result. It would be difficult to decide what is a result of pure rotational damping, and what is a result of a flapping–rotation coupled 'rotational' aerodynamic force.

2.6.5. *Added-mass effects*

The concept of 'added mass' (or 'virtual' mass) is best understood as the aerodynamic forces and moments that are dependent upon a body's acceleration, be it translational or rotational. In the strictest sense, added-mass forces and moments are only those that result from the solution of the Euler equations without circulation (potential flow). Aerodynamic forces and moments dependent upon acceleration may also occur as a result of viscous effects, a notable example being the Basset force (Yih 1977), which represents forces that occur due to an acceleration-dependent lag in boundary-layer development, though all viscous-based acceleration forces are sometimes called Basset forces. Without strong evidence of their importance and an accurate method to predict them, Basset forces will not be accounted for separately. Their influence, if any, will find its way into the standard aerodynamic force and moment coefficients, which are derived from experiments.

There is no analytical solution to the potential-flow equations for a general two-dimensional wing planform moving in a three-dimensional fashion. However, the potential-flow solution for an arbitrary two-dimensional body translating and rotating in two dimensions is well known. Application of this solution easily gives the added-mass forces and moments for a thin wing section. From Sedov (1965),

$$\left.\begin{aligned} Z_0 &= -\lambda_z \dot{W}_0 - \lambda_{zy} \dot{V}_0 - \lambda_{z\omega} \dot{\omega}_x - \omega_x(\lambda_{zy} W_0 + \lambda_y V_0 - \lambda_{y\omega} \omega_x), \\ Y_0 &= -\lambda_{zy} \dot{W}_0 - \lambda_y \dot{V}_0 - \lambda_{y\omega} \dot{\omega}_x + \omega_x(\lambda_z W_0 + \lambda_{zy} V_0 + \lambda_{z\omega} \omega_x), \\ \mathfrak{M}_o &= -\big[\lambda_{z\omega} \dot{W}_0 + \lambda_{y\omega} \dot{V}_0 + \lambda_\omega \dot{\omega}_x + \lambda_{zy}\big(V_0^2 - W_0^2\big) + (\lambda_z - \lambda_y) W_0 V_0 \\ &\quad + \omega_x(\lambda_{z\omega} V_0 - \lambda_{y\omega} W_0)\big], \end{aligned}\right\} \tag{2.40}$$

where Z_0 and Y_0 are the added-mass forces (per unit depth) in the z- and y-directions, and $\mathfrak{M}_o$ is the added-mass moment per unit depth. W_0 and V_0 are the components of the velocity of the wing at its axis of rotation (see figure 3). The λ_{ab} terms are the 'coefficients of added mass'. Repeated subscripts are dropped. The wing section shown in figure 3 has effectively zero thickness and a rotational-axis offset from the midpoint by y_h, which can be expressed non-dimensionally as

$$\hat{y}_h(\hat{r}) = \tfrac{1}{2}\hat{c}(\hat{r}) - \hat{y}_{LE}(\hat{r}) - \hat{y}_r. \tag{2.41}$$

The non-zero added-mass coefficients for a thin flat wing section are

$$\left.\begin{aligned} \lambda_z &= \pi\rho a^2, \\ \lambda_{z\omega} &= -\pi\rho a^2 y_h, \\ \lambda_\omega &= \pi\rho a^2 y_h^2 + \tfrac{1}{8}\pi\rho a^4, \end{aligned}\right\} \tag{2.42}$$

where a is the semi-chord and ρ is the density of the surrounding air. Note that many of the terms in (2.40) are 'cross-term' accelerations and not pure rotations. These will not be considered, as they will duplicate existing blade-element terms with similar forms, such as the rotational force and damping terms. The validity of these terms (as well as the pure acceleration terms) is already in question, as this formulation assumes fully attached irrotational flow in two dimensions. After eliminating cross-terms and terms with zero-valued coefficients, (2.40) is reduced to

$$\left.\begin{aligned} Z_0 &= -\lambda_z \dot{W}_0 - \lambda_{z\omega}\dot{\omega}_x, \\ Y_0 &= 0, \\ \mathfrak{M}_\circ &= -\lambda_{z\omega}\dot{W}_0 - \lambda_\omega \dot{\omega}_x. \end{aligned}\right\} \tag{2.43}$$

The normal acceleration is given by $\dot{W}_0 = -r(\dot{\omega}_y - \omega_x\omega_z)$. Substitution and radial integration yields

$$M_{x,am} = -\left(\frac{\pi}{4}\rho\bar{c}^3 R^2 \hat{I}_{xy,am}\right)(\dot{\omega}_y - \omega_x\omega_z) - \left(\frac{\pi}{4}\rho\bar{c}^4 R \hat{I}_{xx,am}\right)\dot{\omega}_x, \tag{2.44}$$

where

$$\left.\begin{aligned} \hat{I}_{xy,am} &= \int_0^1 (\hat{r} + \hat{x}_r)\hat{c}(\hat{r})^2 \hat{y}_h(\hat{r})\,\mathrm{d}\hat{r}, \\ \hat{I}_{xx,am} &= \int_0^1 \hat{c}(\hat{r})^2 \left(\hat{y}_h(\hat{r})^2 + \tfrac{1}{32}\hat{c}(\hat{r})^2\right)\mathrm{d}\hat{r}. \end{aligned}\right\} \tag{2.45}$$

A similar integration yields the added-mass term, $F_{z,am}$.

3. Passive-rotation experiments and analysis

Using the blade-element method to estimate aerodynamic torques raises two major concerns. The first is whether the quasi-steady approximation is overly limiting. Wake-capture effects and other path-dependent phenomena must be negligible. The second concern is the validity of force and moment coefficients. The method is useless if different force and moment coefficients are required for every operating condition and wing shape. More precisely, aerodynamic coefficients must change little for reasonable changes in flapping frequency, flapping kinematics and wing shape. Quantification of 'little' and 'reasonable' is arbitrary.

Experiments are needed to assess the performance of the blade-element method in predicting time-dependent forces and moments. If wing kinematics and forces are measured simultaneously, force coefficients for each wing and kinematics configuration can be extracted. If the experiments are done with passively rotating wings, the validity of (2.15) can be assessed directly.

3.1. *Experimental set-up and calibration*

A testing set-up, illustrated in figure 4, was constructed for the synchronized measurement of three-degree-of-freedom flapping kinematics ($\phi(t)$, $\theta(t)$, $\psi(t)$) and

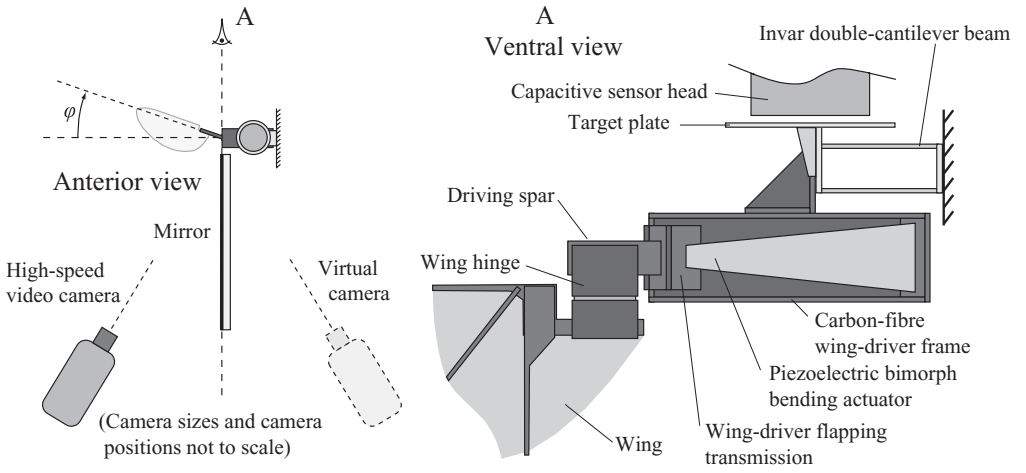

FIGURE 4. Experimental set-up for measuring lift forces and capturing wing motion using high-speed video. The wing driver is attached to an Invar double-cantilever beam. The beam deflection is measured by a capacitive displacement sensor. A mirror generates a second camera view, allowing stereoscopic reconstruction.

lift forces on robotically driven wings. Although all wings tested here are of artificial construction, the set-up does not preclude the use of natural wings. Kinematics are determined *a posteriori* using stereoscopic reconstruction of high-speed video recordings. The wing-driver mechanism is mounted on the end of a double-cantilever beam. The beam's deflection is measured with a capacitive displacement sensor. To the authors' knowledge, these are the first reported experiments that measure three-degree-of-freedom flapping kinematics, synchronized to real-time force measurements for insect-scale flapping wings.

The wing is flapped using a piezoelectric bimorph actuator, of the type described by Wood, Steltz & Fearing (2005), mounted in a carbon-fibre frame. The linear displacement of the drive actuator is mapped to an angular flapping motion using a transmission mechanism of the type described by Wood (2008). The actuator is made as small as possible to minimize the effective mass of the beam–driver system, thus maximizing sensor bandwidth.

The double-cantilever beam is laser-cut and folded from 150 μm Invar sheet (Wood, Cho & Hoffman 2009). Abutting folded edges are soldered together. The double-cantilever topology ensures that the beam deflects linearly without rotation. The dual beams are 7 mm long, 4 mm wide and spaced vertically by 3 mm. The 10 mm diameter capacitive sensor target plate, also laser-cut from Invar sheet, is attached to the end of the beam with a pair of triangular support ribs. These ribs also serve to stiffen the end-plate of the beam to maintain the desired built-in boundary condition. The mass of the wing driver (frame, actuator, transmission) is approximately 150 mg. Using simple-beam theory, the predicted sensor resonant frequency is 950 Hz. This includes the effect of wing-driver mass, target plate and support rib mass, and the theoretical effective mass of the sensor beam. The measured resonant frequency of the system, determined by impulse testing, is 810 Hz. All reported force data have been post-processed with a high-order zero-phase 750 Hz digital low-pass filter. The force sensor was calibrated using multi-point static loading with known masses. No attempts at dynamic calibration (cf. Graetzel 2008) have been made. Sensor output

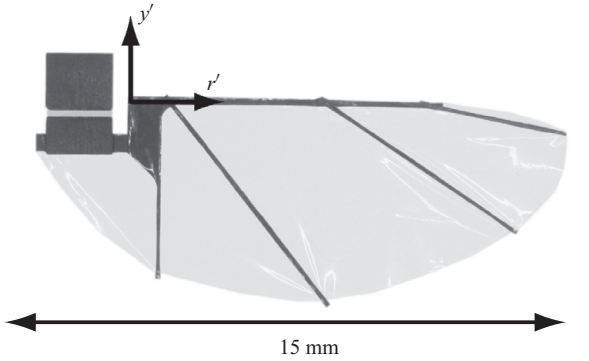

FIGURE 5. A wing of this design is used for all experimental data presented here, with either the longer wing hinge for the 70 Hz flapping case (shown here) or the shorter hinge for all other cases. Wing length is 15 mm, measured from 'shoulder' to tip. The spars are 80 μm thick carbon fibre, bonded to the wing membrane, 1.5 μm thick polyester film.

is 1.04 mg mV^{-1}, with a measured noise floor of 1.5 mV, at full bandwidth. All force data are reported as mass-equivalent using a gravity acceleration of 9.8 m s^{-2}.

A high-speed video camera is used to record wing motion. All video recordings were captured at 10 000 frames per second, with exposure times of 30 μs. As shown in figure 4, a mirror provides a second camera view. The camera points towards the wing from approximately $\phi = -60°$. The camera is positioned at least 150 mm away from the wing (10 wing lengths) to minimize aerodynamic disturbance. The primary view and virtual-camera view are illuminated by backlight; fibre-optic light guides direct light from standard tungsten halogen illuminators onto diffusion screens, each positioned 150 mm behind the wing. The ground plane (optical table) is located 200 mm below the wing.

A computer with a real-time control board sends drive signals to high-voltage amplifiers, which drive the piezoelectric actuator. The same board issues camera trigger signals and samples the capacitive displacement sensor at 5 kHz. Synchronization between the trigger signal and the camera frame buffer was confirmed by recording a light-emitting diode being driven directly by the trigger signal. Synchronization between video frames and the force signal was confirmed by recording an impulse impact on the driving spar and matching the time-of-impact video frame with the force signal.

3.2. *Extracting flapping kinematics*

Stereoscopic calibration of the camera set-up is accomplished using the methods of Zhang (2000) and Bouguet (2008). Several images of a draughts board with known dimensions are taken. The draughts board is placed at several positions and with several orientations to the camera, with care that the complete pattern is seen by both the real and virtual camera. The images are used to fit a lens-distortion model and the relative positioning between the two cameras is calculated. The resulting calibration maps row–column pixel coordinates for the real and virtual images (corresponding to the same physical point) to a three-dimensional location relative to the real camera.

Three points are tracked on the wing, with their coordinates used to define an instantaneous mean wing plane for each video frame. Figure 5 shows a photograph of the wing used for all experiments presented here. The first, second and fourth (proximal to distal) spar ends are used for the tracking points. A normal vector

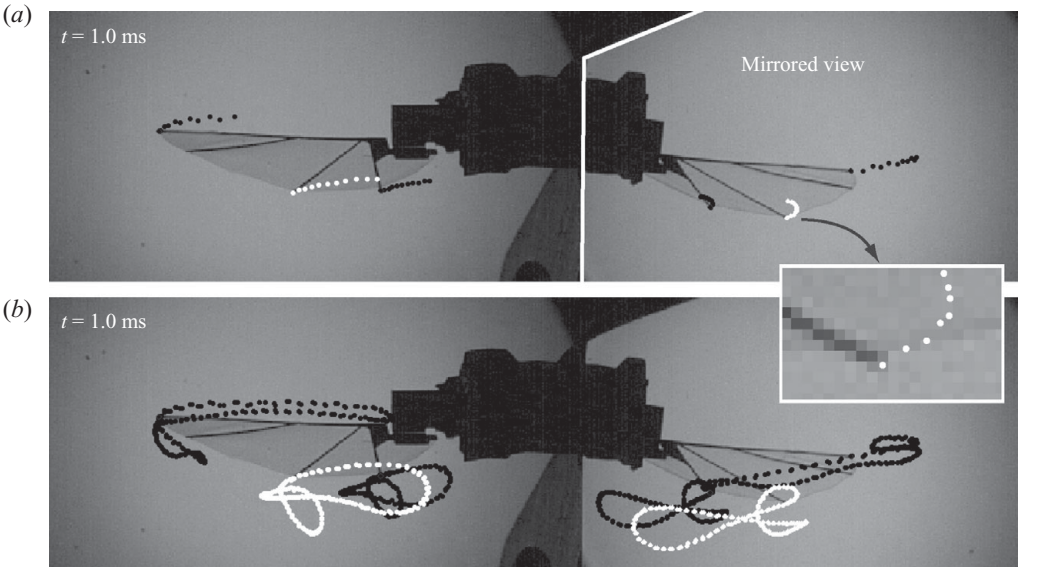

FIGURE 6. The 11th frame of the baseline 100 Hz case is shown in both images. The image in (*a*) highlights the mirror edge and labels the real and virtual images, and shows tracked spar endpoints for the first 11 frames. The image in (*b*) shows tracking results from a complete 200-frame, two-period sequence. The high degree of periodicity is evident from the pairwise clustering of the points. The spar ends are tracked manually, for each frame, on a sub-pixel basis.

defined by these points is projected onto fixed axes to extract the flapping, out-of-plane and rotational angles. Figure 6 shows a sample frame from a captured video recording. For all experiments carried out, the wing stayed very flat and did not deviate very far from the rigid-body ideal. Figure 7 shows a frame sequence which is characteristic of the maximal amount of wing fluttering and spar bending observed. While in these experiments the intent was to suppress wing deformations, these tracking techniques could be easily used to reconstruct higher order oscillation and deflection modes by tracking more points.

Each video recording consists of two full flapping periods. The hinge line (torsional axis) is determined from an image of the wing at rest; it is identified as the midline of the wing-hinge flexure. The position and orientation of the hinge line is then determined by offset in local coordinates for each frame in the flapping sequence. A plane is fitted through the track left by the hinge line, over the full time sequence, to define the so-called mean stroke plane, which establishes a reference for defining out-of-plane motion, $\theta(t)$. The wing orientation calculated from an image of the wing at rest is used to define the flapping-angle origin ($\phi = 0$). A sphere is fitted to the point cloud left by the track of the distal edge of the wing hinge to determine the radial offset of the wing from the centre of rotation.

All plots of measured angular trajectories are shown unfiltered, in degrees. However, when derivatives are calculated for use by the blade-element method, filtering is applied to prevent excessive noise.

3.3. *Experimental results*

All of the following experiments use the same wing design. The two experiments flapping at 100 Hz use the same 'short' wing hinge, and the 70 Hz case uses the

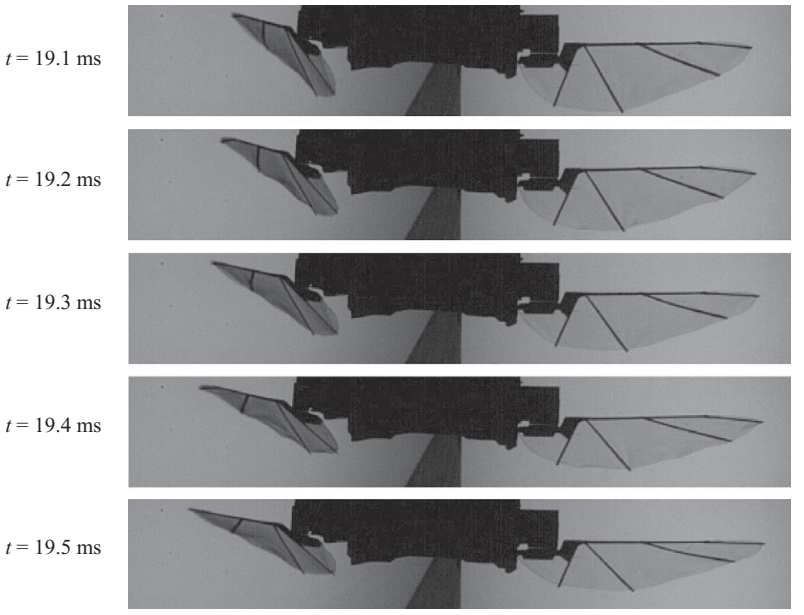

FIGURE 7. This sequence, taken from the 100 Hz baseline case, shows observed membrane fluttering and spar bending. The two most distal spars are clearly seen to flex between the fourth and fifth frames.

'long' hinge. Detailed specifications for the wing and the wing hinge are given in the Appendix.

The measured values of ψ and $\dot{\psi}$ at $t = 0$ provide the initial condition. All calculations to predict the rotational trajectory of the wing are made by integration of (2.15). This means that measurements of out-of-plane deviation, $\theta(t)$, contribute to the solution. However, all experiments presented here do not contain significant out-of-plane motion, as the flapping mechanism does not support it. In practice, trajectories predicted by (2.16) are very similar. The small amount of out-of-plane deviation that does occur is a result of wing-hinge compliance. While designed to be much more compliant in the rotational axis, the off-axis compliance is enough to allow a few degrees out-of-plane motion when under high load.

Lift coefficient, $C_{L_{max}} = 1.7$, is used for all calculations. This value provides good general agreement with all experiments performed, and is very close to 1.8, the classic *Drosophila* value. Drag data from Dickinson *et al.* (1999) and the $\hat{d}_{cp}(\alpha)$ trend reported by Dickson *et al.* (2006), given in (2.26), are used, as none of the current experiments directly measure these values. The same rotational damping coefficient ($C_{rd} = 5.0$) was used for all calculations. Unless otherwise noted, no rotational aerodynamic forces or rotational added inertia terms were applied (though the added-mass lift force is included).

In the following plots, unless otherwise noted, the term 'lift' indicates the reaction force of the wing on the drive spar, i.e.

$$F_N = F_{aero,X'} - m\, a_{X'}, \tag{3.1}$$

where F_N is the total lift, $F_{aero,X'}$ is the projection of the total aerodynamic force vector onto the X'-axis, m is the wing mass and $a_{X'}$ is the linear acceleration of the centre of mass of the wing. It is important to note that 'lift' in the current sense

is different from 'lift' in the sense of the blade-element method. The unit vector $\boldsymbol{e}_L$ used in blade-element calculations always points normal to the instantaneous stroke plane, rather than the mean stroke plane, which is the plane of reference for F_N and $F_{aero,X'}$.

All measured mean lift values are obtained by averaging over 10 periods, while the calculated lift values are derived from the kinematics captured during the first two of those periods. The inertial component has zero mean when the wing motion is perfectly periodic, but the instantaneous values of the inertial contribution are non-trivial, and must be added to aerodynamic lift predictions when comparing to experimental measurements.

In general, working at-scale poses the extra challenge of dealing with wing inertial forces, which are typically of the same order as the aerodynamic forces. Subtracting them out requires high-quality kinematics measurements to extract the crucial angular accelerations. Measuring wing mass with an electrobalance is easy, but measuring inertias and products of inertia is not trivial. The I_{xx} and I_{xy} values used here were calculated from a three-dimensional computer model of the wing, using measured material densities. The wing centre of mass was also calculated from this model. As a check, measured masses were confirmed to agree with predicted masses from the model.

The hinge stiffness is simply calculated using (2.12), using the hinge geometry parameters and the specification-sheet modulus for the polyimide film used to make the hinge flexure. Potential hinge stiffness nonlinearity and damping have not been characterized.

3.3.1. *Baseline 100 Hz flapping experiment*

The first case (the 'baseline') examines passive rotation at 100 Hz. The flapping amplitude, Φ, is 108°. Figure 8(a) plots the measured kinematics and predicted rotation. The out-of-plane motion is only a few degrees. The transmission mechanism is not perfectly symmetric, and real-time position feedback is not currently available. The downstroke experiences larger lift forces, as the wing velocity is slightly higher then. The mean measured lift is 71.6 mg, and the calculated lift is 73.7 mg.

Figure 9 shows predicted rotation, for the same case, with different combinations of the $I_{xx,am}$ and $I_{xy,am}$ terms. It appears that inclusion of the $I_{xy,am}$ term improves the prediction of the maximum amount of negative rotation, but the agreement is compromised in other areas. These differences were investigated in other experimental data sets, and no consistent improvement for any of these added inertia terms could be found. This does not mean that they are not important, but their contribution is simply less than the uncertainty introduced by other factors, such as the centre-of-pressure location and nonlinear hinge compliance.

Figure 10 shows each component of the predicted lift force. It is clear that subtracting the inertial contribution is critical for analysing the aerodynamic contribution. At the end of a stroke, when the wing flips, wing velocity, and thus lift, is low, while vertical acceleration of the centre of mass is high (centripetal acceleration), leading to an inertial reaction peak (negative lift peak). This effect is more or less relevant depending on the mass of the wing, rate of flip and other factors.

From figure 11, it is clear that an additional rotational aerodynamic damping term is critical to the prediction of realistic rotational dynamics. As mentioned earlier, refinement of this component will require experiments that can directly measure rotational torques.

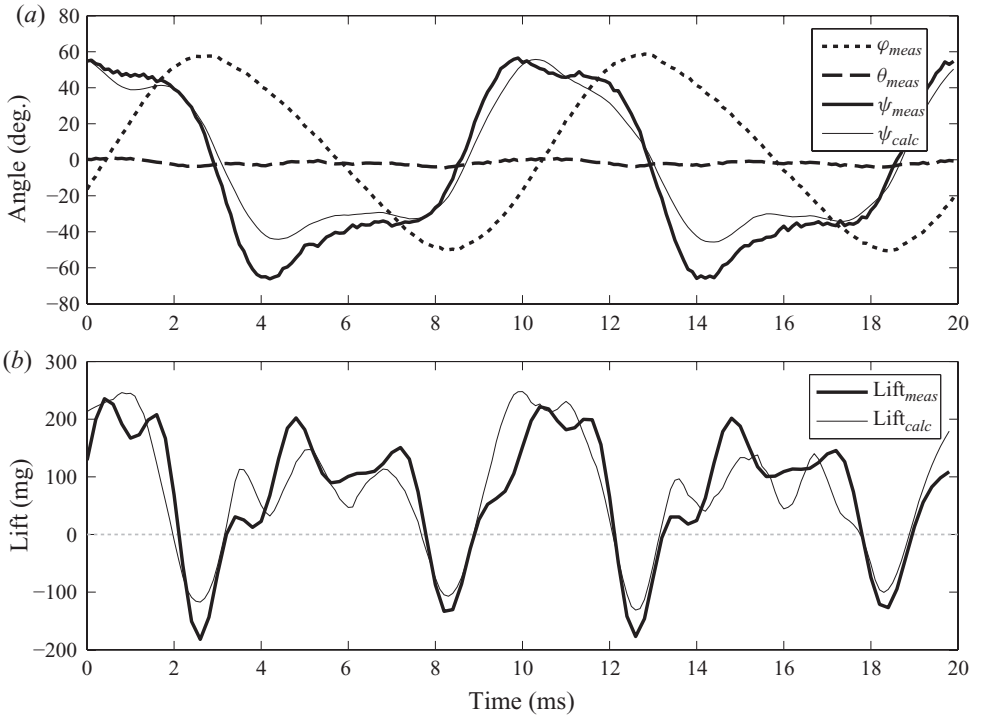

FIGURE 8. Baseline 100 Hz flapping case (short hinge). (*a*) Measured kinematics are plotted unfiltered. Predicted wing rotation does not include any rotational aerodynamic force or rotational added inertia terms. (*b*) Predicted lift includes inertial reaction of the wing and theoretical added-mass lift.

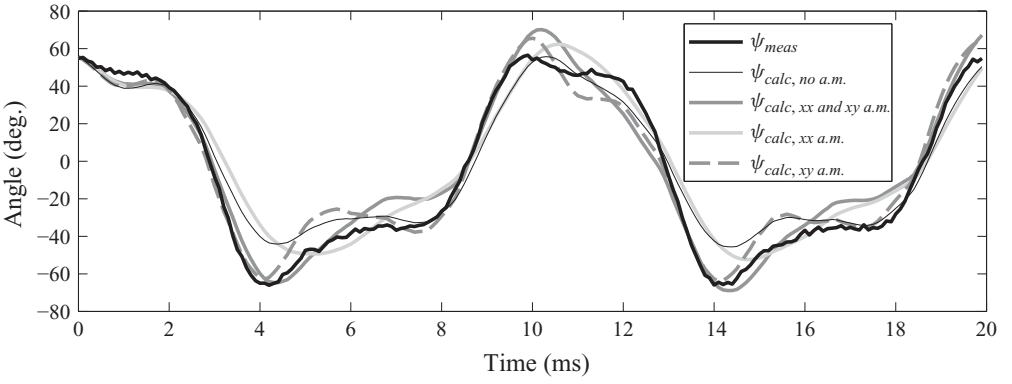

FIGURE 9. Baseline 100 Hz flapping case (short hinge). Measured wing rotation and predicted wing rotation using each combination of the theoretical rotational added inertia terms.

3.3.2. *Split-cycle flapping experiment*

The next experiment presented uses the same wing, with the same wing hinge, flapping at the same fundamental frequency. However, the full flapping period is a concatenation of a longer duration upstroke and a shorter duration downstroke. The upstroke-to-downstroke duration ratio, called τ_{ss}, is 0.62 in this case. The asymmetry in $\phi(t)$ is readily apparent in figure 12. This type of flapping is called 'split cycle',

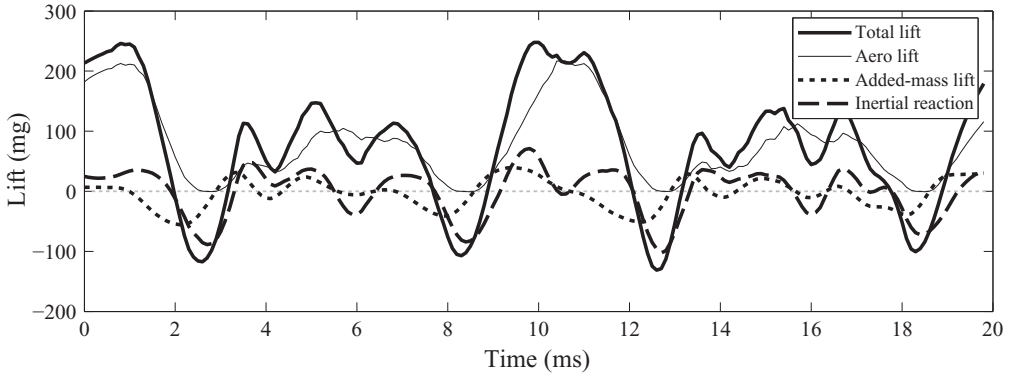

FIGURE 10. Baseline 100 Hz flapping case (short hinge). The predicted total lift force is broken down into constituent components.

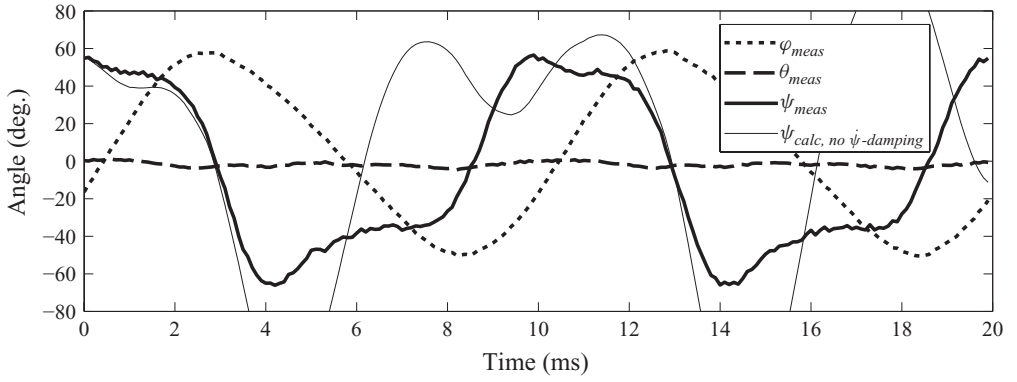

FIGURE 11. Baseline 100 Hz flapping case (short hinge). Measured (all) and predicted (rotational only) kinematics are again plotted, except that the prediction does not include a pure rotational damping term.

which is aimed at breaking the upstroke–downstroke symmetry to create net roll moments (roll in the sense of figure 2). This technique was proposed by Doman & Oppenheimer (2009) as a method to control roll for a flapping-wing robotic insect. For this case, the measured lift is 71.2 mg, almost identical to the baseline case. The predicted lift, using the same lift coefficient as the baseline case, is 75.7 mg. Since roll torques were not measured, the effectiveness in generating a net moment cannot be assessed, but it is clear that the rotational kinematics can be made very asymmetric without changes in mean lift, while operating under the restrictions of a passively rotating system.

Agreement between the predicted and measured lift forces, on a time-varying as well as mean-value basis, is excellent, even though the peak lift force in the split-cycle case is almost twice that of the baseline case. The blade-element method, in this case, is highly tolerant of drastic changes in flapping and rotational kinematics. In spite of the uncertainties in drag coefficients, centre-of-pressure location, damping and rotational forces, the approximate values based on published data for *Drosophila* lead to good predictions of passive-rotation dynamics.

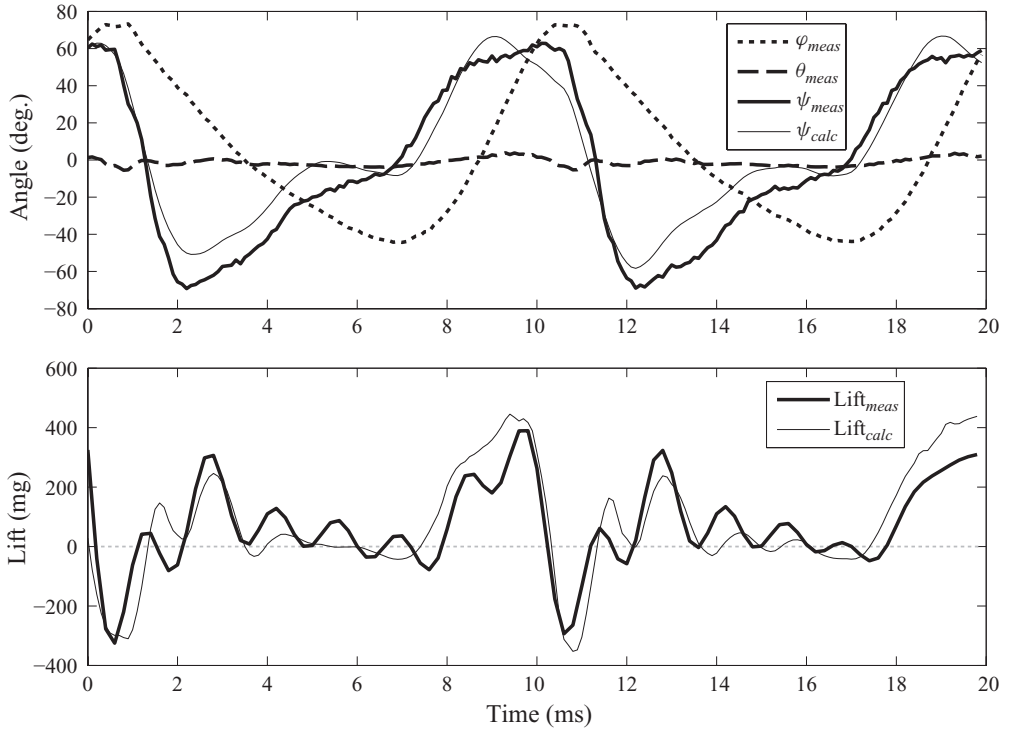

FIGURE 12. 100 Hz flapping case (short hinge), now with $\tau_{ss} = 0.62$ split-cycle flapping-angle kinematics.

3.3.3. *70 Hz flapping experiment*

For the final experiment, the wing hinge was lengthened, allowing the wing to achieve sufficient rotation when flapped at 70 Hz. The total flapping angle is also reduced to 90°. The measured lift is 30.4 mg, and the predicted lift is 26.6 mg (same coefficients as all other cases). Trajectory and force results are plotted in figure 13. There appears to be a small phase discrepancy between the measured and predicted rotation angle, while the amplitude prediction is excellent. On the other hand, the baseline case showed excellent phase agreement, with small disagreements at times in amplitude. The various model uncertainties are not small enough to draw general conclusions on the sources of these discrepancies. It is possible that wake-capture effects and rotational aerodynamic effects are contributing to the observed forces, but, at this time, the data available are not fine enough to separate these effects from other aerodynamic uncertainties. It is clear, at least for the range of cases examined here, that exclusion of these effects does not preclude accurate estimates of passive-rotation trajectories.

4. Conclusions and future work

In these experiments, the predicted and measured lift forces show excellent agreement, both in mean value and detailed time history. These predictions were consistent across large changes in flapping kinematics, flapping frequency and flapping amplitude, without any changes to model coefficients. These experiments reveal that coping with inertial wing forces is an important challenge when working

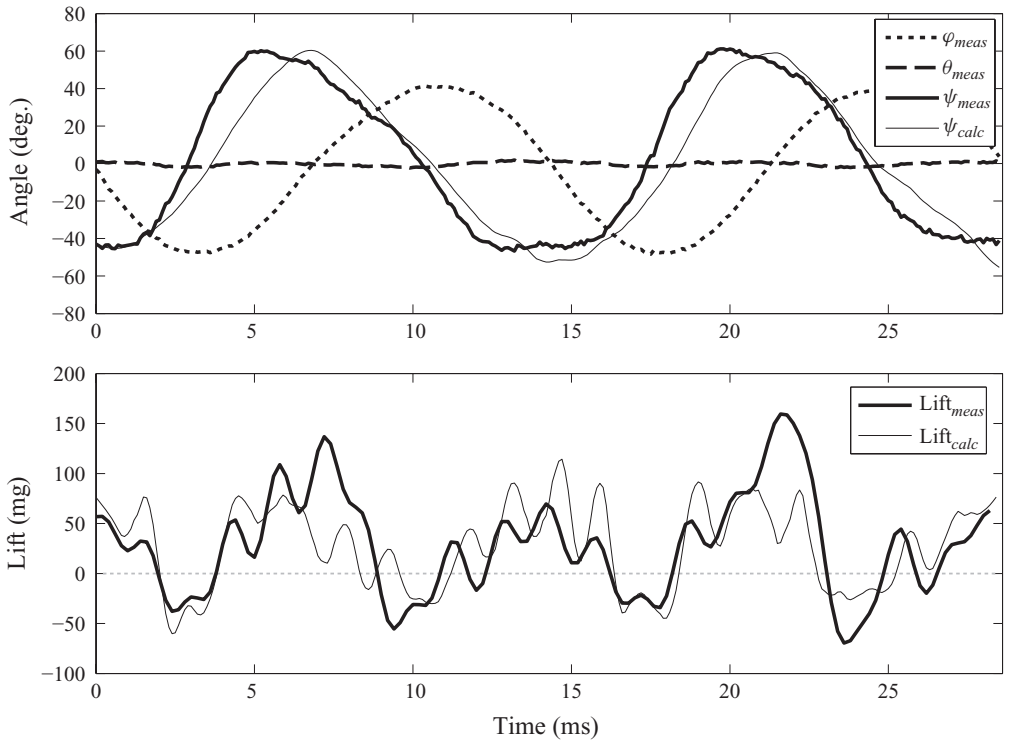

FIGURE 13. 70 Hz flapping case (long hinge). A longer hinge (more hinge compliance) allows an appropriate amount of wing rotation when flapping at a lower frequency.

with actual-size wings. Minimizing the influence of these inertial forces in isolating aerodynamic loads will be critical for continued success in at-scale studies of flapping-wing aerodynamics. It is difficult to quantify the agreement of measured kinematics with passive-rotation predictions. Qualitatively, the rotational dynamics were well captured, including sub-period modes. Quantitatively, peak rotational amplitudes, rates and phases showed good agreement with measured values. Demonstration of asymmetric split-cycle kinematics, without reductions in lift force, strongly motivate further investigation of this wing-control strategy.

Improvements in passive-rotation trajectory predictions will not come without a great deal of work in measuring and characterizing flight forces and moments. Rotational moments, in particular, must be measured for a variety of wing shapes, sizes and flapping profiles. In spite of this lack of data, the blade-element method, when used with published data, provides very good predictions of passive-rotation trajectories. It is eminently useful in the design of robotic wing hinges. These methods can now be used, with confidence, to study achievable optimal kinematics under the reduced input control available with a passive-rotation system.

These experiments lay the groundwork for exciting future studies of natural insect wings and artificial wings that include distributed compliance. This work has demonstrated the measurement of real-time forces and three-dimensional kinematics for at-scale flapping wings. Because the wings are driven mechanically, it is possible to precisely control experimental parameters in ways not possible when working with live insects. Since the experiments are at-scale, actual insect wings can be tested. The demonstrated quality of the measured forces motivates future work focused

directly on the aerodynamics. Methods to more precisely control flapping kinematics, combined with flow-visualization techniques, will complement existing capabilities in measuring and understanding detailed wing deformations and real-time forces.

The authors gratefully acknowledge support from the US Army Research Laboratory, under award number W911NF-08-2-0004, and the US Air Force Office of Scientific Research, under award number FA9550-09-1-0156.

Appendix. Experimental parameters

The wing, pictured in figure 5, is designed to have a shoulder-to-tip distance of 15 mm, $\mathcal{R} = 3.5$, $\hat{r}_1 = 0.5$ and $\hat{r}_2 = 0.56$. Measured from the $r'y'$-origin, $R = 11.95$ mm, $x_r = 3.19$ mm and $y_r = 0.73$ mm. Wing mass is 0.91 mg, with $I_{xx} = 1.70$ mg mm^2 and $I_{xy} = 3.50$ mg mm^2. The centre of mass is located at $x_{cm} = 5.74$ mm and $y_{cm} = -1.31$ mm, relative to O'. The 'short' wing hinge has the following parameters: $L_h = 70\,\mu$m, $w_h = 1.8$ mm, $t_h = 7.6\,\mu$m and $E_h = 2.5$ GPa. The 'long' hinge is 175 μm long. The hinge-flexure material in both cases is polyimide film.

The wing leading-edge shape, $\hat{y}_{LE}(\hat{r})$, can be digitized from figure 5. From $\hat{r} = 0$ to $\hat{r} = 0.75$, $\hat{y}_{LE} = 0$. Outboard of that, an elliptical profile was originally intended, but the use of straight wing spars necessitated modification of this profile to avoid creating unsupported regions of the leading-edge membrane. The chosen profile attempts to balance the need to support the membrane with the desire to create a reasonably rounded tip.

These wing parameters are similar to those of *Eristalis tenax*, as reported by Ellington (1984). Reported parameters are $R = 11$ mm, $\hat{r}_1 = 0.48$, $\hat{r}_2 = 0.54$, $\mathcal{R} = 3.6$ and a wing mass between 0.90 and 1.05 mg. For the same species, Ennos (1988*b*) reports a torsional axis 15 % behind the leading edge and a centre of mass 30 % back. Compare this to values of 17 % and 47 % for the present wing.

The wing spars are laser-cut from unidirectional carbon fibre, pre-impregnated with a cyanate ester resin. The nominal thickness of this 'prepreg' material is 80 μm. The wing membrane is laser-cut from 1.5 μm polyester film. The spars are then oven-cured and bonded to the membrane while under pressure.

REFERENCES

Andersen, A., Pesavento, U. & Wang, Z. J. 2005 Unsteady aerodynamics of fluttering and tumbling plates. *J. Fluid Mech.* **541**, 65–90.

Bergou, A. J., Xu, S. & Wang, Z. J. 2007 Passive wing pitch reversal in insect flight. *J. Fluid Mech.* **591**, 321–337.

Bouguet, J.-Y. 2008 *Camera Calibration Toolbox for Matlab*. Available at: http://www.vision.caltech.edu/bouguetj/calib_doc/.

Daniel, T. L. & Combes, S. A. 2002 Flexing wings and fins: bending by inertial or fluid-dynamic forces? *Intgr. Comp. Biol.* **42** (5), 1044–1049.

Dickinson, M. H., Lehmann, F.-O. & Sane, S. P. 1999 Wing rotation and the aerodynamic basis of insect flight. *Science* **284**, 1954–1960.

Dickson, W. B., Straw, A. D., Poelma, C. & Dickinson, M. H. 2006 An integrative model of insect flight control. In *Proceedings of the AIAA Aerospace Sciences Meeting and Exhibit*, Reno, NV.

Doman, D. B. & Oppenheimer, M. W. 2009 Dynamics and control of a minimally actuated biomimetic vehicle: Part I. Aerodynamic model. In *Proceedings of the AIAA Guidance, Navigation, and Control Conference*, San Francisco, CA.

Dudley, R. 2000 *The Biomechanics of Insect Flight: Form, Function, Evolution*. Princeton University Press.

Ellington, C. P. 1984 The aerodynamics of insect flight. II. Morphological parameters. *Phil. Trans. R. Soc. Lond.* B **305**, 17–40.

Ennos, A. R. 1988*a* The importance of torsion in the design of insect wings. *J. Exp. Biol.* **140**, 137–160.

Ennos, A. R. 1988*b* The inertial cause of wing rotation in Diptera. *J. Exp. Biol.* **140**, 161–169.

Fry, S. N., Sayaman, R. & Dickinson, M. H. 2003 The aerodynamics of free-flight maneuvers in *Drosophila*. *Science* **300**, 495–498.

Graetzel, C. 2008 MEMS & high speed vision: development and application to reverse-engineer *Drosophila* flight control. PhD thesis, ETH Zurich.

Graetzel, C. F., Fry, S. N., Beyeler, F., Sun, Y. & Nelson, B. J. 2008 Real-time microforce sensors and high speed vision system for insect flight control analysis. In *Experimental Robotics: The 10th International Symposium on Experimental Robotics*, p. 451. Springer.

Lentink, D. & Dickinson, M. H. 2009 Rotational accelerations stabilize leading edge vortices on revolving fly wings. *J. Exp. Biol.* **212** (16), 2705.

Pesavento, U. & Wang, Z. J. 2009 Flapping wing flight can save aerodynamic power compared to steady flight. *Phys. Rev. Lett.* **103** (11), 118102.

Ristroph, L., Berman, G., Bergou, A., Wang, Z. J. & Cohen, I. 2009 Automated hull reconstruction motion tracking (HRMT) applied to sideways maneuvers of free-flying insects. *J. Exp. Biol.* **212**, 1324–1335.

Sane, S. P. 2003 The aerodynamics of insect flight. *J. Exp. Biol.* **206** (23), 4191.

Sane, S. P. & Dickinson, M. H. 2002 The aerodynamic effects of wing rotation and a revised quasi-steady model of flapping flight. *J. Exp. Biol.* **205**, 1087–1096.

Sedov, L. I. 1965 *Two-Dimensional Problems in Hydrodynamics and Aerodynamics*. Interscience.

Walker, S. M., Thomas, A. L. R. & Taylor, G. K. 2009 Photogrammetric reconstruction of high-resolution surface topographies and deformable wing kinematics of tethered locusts and free-flying hoverflies. *J. R. Soc. Interface* **6** (33), 351.

Wang, Z. J. 2000 Two-dimensional mechanism for insect hovering. *Phys. Rev. Lett.* **85** (10).

Wang, Z. J., Birch, J. & Dickinson, M. H. 2004 Unsteady forces and flows in low Reynolds number hovering flight: two-dimensional computations *vs* robotic wing experiments. *J. Exp. Biol.* **207**, 449.

Wood, R. J. 2007 Design, fabrication, and analysis of a 3 DOF, 3 cm flapping-wing MAV. In *IEEE/RSJ International Conference on Intelligent Robots and Systems*, pp. 1576–1581.

Wood, R. J. 2008 The first takeoff of a biologically inspired at-scale robotic insect. *IEEE Trans. Robot.* **24**, 341–347.

Wood, R. J., Cho, K. J. & Hoffman, K. 2009 A novel multi-axis force sensor for microrobotics applications. *Smart Mater. Struct.* **18**, 125002.

Wood, R. J., Steltz, E. & Fearing, R. S. 2005 Nonlinear performance limits for high energy density piezoelectric bending actuators. In *IEEE International Conference on Robotics and Automation*, pp. 3633–3640.

Wu, J. H. & Sun, M. 2004 Unsteady aerodynamic forces of a flapping wing. *J. Exp. Biol.* **207**, 1137–1150.

Yih, C. S. 1977 *Fluid Mechanics: A Concise Introduction to the Theory*. West River Press.

Young, J., Walker, S. M., Bomphrey, R. J., Taylor, G. K. & Thomas, A. L. R. 2009 Details of insect wing design and deformation enhance aerodynamic function and flight efficiency. *Science* **325** (5947), 1549–1552.

Zhang, Z. 2000 A flexible new technique for camera calibration. *IEEE Trans. Pattern Anal. Mach. Intell.* **22** (11), 1330–1334.